

Two-dimensional topological quantum walks in the momentum space of structured light: supplementary material

ALESSIO D'ERRICO¹, FILIPPO CARDANO^{1,*}, MARIA MAFFEI^{1,2}, ALEXANDRE DAUPHIN^{2,*}, RAOUF BARBOZA¹, CHIARA ESPOSITO¹, BRUNO PICCIRILLO¹, MACIEJ LEWENSTEIN^{2,3}, PIETRO MASSIGNAN^{2,4,*}, AND LORENZO MARRUCCI^{1,5}

¹Dipartimento di Fisica, Università di Napoli Federico II, Complesso Universitario di Monte Sant'Angelo, Via Cintia, 80126 Napoli, Italy

²ICFO – Institut de Ciències Fotoniques, The Barcelona Institute of Science and Technology, 08860 Castelldefels (Barcelona), Spain

³ICREA – Institució Catalana de Recerca i Estudis Avançats, Pg. Lluís Companys 23, 08010 Barcelona, Spain

⁴Departament de Física, Universitat Politècnica de Catalunya, Campus Nord B4-B5, 08034 Barcelona, Spain

⁵CNR-ISASI, Institute of Applied Science and Intelligent Systems, Via Campi Flegrei 34, 80078 Pozzuoli (NA), Italy

*Corresponding authors: filippo.cardano2@unina.it, alexandre.dauphin@icfo.eu, pietro.massignan@upc.edu

Published January 23, 2020

This document provides supplementary information to "Two-dimensional topological quantum walks in the momentum space of structured light," <https://doi.org/10.1364/OPTICA.365028>. We provide technical details about materials and methods used for our experiment. We provide a description of the photonic modes that we exploit to perform our simulations, and describe more carefully the experimental setup. We describe technical aspects of the experimental methodology, and analyze in details the topological features of our quantum walk. Finally, we discuss limitations of our setup and possible solutions, and provide further experimental data.

1. PHOTONIC SPATIAL MODES FOR THE ENCODING OF THE WALKER DEGREE OF FREEDOM

A. Gaussian modes encoding single walker positions

The state $|\mathbf{m}, \phi\rangle$ of a walker is encoded in our set-up in a light beam described by Eq.1 in the main manuscript

$$|\mathbf{m}, \phi\rangle = A(x, y, z) e^{i[\Delta k_{\perp}(m_x x + m_y y) + k_z z]} \otimes |\phi\rangle, \quad (\text{S1})$$

where $\mathbf{m} = (m_x, m_y)$ are the integer coordinates giving the discrete position of the walker, and the light's polarization $|\phi\rangle$ encodes the state of the coin of the walker. The spatial profile of the beam is determined by the Gaussian envelope function

$$A(x, y, z) = \frac{w_0}{w(z)} e^{-\frac{x^2 + y^2}{w(z)^2}} e^{ik \frac{x^2 + y^2}{2R(z)}} e^{-i\zeta(z)}, \quad (\text{S2})$$

where $k = 2\pi/\lambda$ is the wavenumber, and the beam radius $w(z)$, the beam curvature $R(z)$ and the Gouy phase $\zeta(z)$ are defined

as follows:

$$w(z) = w_0 \sqrt{1 + (z/z_0)^2}, \quad (\text{S3})$$

$$R(z) = z[1 + (z_0/z)^2], \quad (\text{S4})$$

$$\zeta(z) = \arctan(z/z_0). \quad (\text{S5})$$

Here $w_0 = w(z=0)$ is the beam radius at the waist position $z=0$, and the parameter $z_0 = \pi w_0^2/\lambda$ is known as Rayleigh range. In our experiment, we set $w_0 = 5$ mm, which yields $z_0 \approx 120$ m, so that across the whole QW setup (about 30 cm long) the beam radius is approximately constant ($w(z) \approx w_0$), and both the Gouy phase $\zeta(z)$ and the inverse beam curvature $1/R(z)$ are entirely negligible.

If we place a converging lens at the end of the quantum walk, in the focal plane the field distribution is proportional to the distribution of the transverse wavevector, that is:

$$A(X, Y) \propto \int_{\Omega} A(x, y, d) e^{i[\Delta k_{\perp}(m_x x + m_y y) + k_z d]} e^{i(Xx + Yy)k/f} dx dy, \quad (\text{S6})$$

where Ω is the transverse plane, d the distance of the lens from the beam waist, f the focal length of the lens, and $\mathbf{R} = (X, Y)$

the spatial coordinates in the focal plane of the lens. It is well known that, independently of the distance d , in the focal plane the field intensity is proportional to the Fourier transform of the field impinging on the lens, that is

$$|A(X, Y)|^2 \propto |g(k_x, k_y)|^2 \quad (S7)$$

where $g(k_x, k_y)$ is the Fourier transform of $A(x, y)$, provided that one sets $X = k_x f/k$ and $Y = k_y f/k$. In the case of a Gaussian beam, we have

$$|A(X, Y)|^2 \propto e^{\left(-2 \frac{(m_x \Delta k_x - kX/f)^2 + (m_y \Delta k_y - kY/f)^2}{\tilde{w}_k^2}\right)}, \quad (S8)$$

with $\tilde{w}_k = 2/w_0$. Thus \tilde{w}_k is a measure of the radius of the spots that appear in the focal plane, provided that one converts the transverse momentum of the photons into a position on the camera. The spatial position \mathbf{R} on the camera is related the transverse momentum of light by the relation

$$\mathbf{R} = \frac{f\lambda \mathbf{k}_\perp}{2\pi}. \quad (S9)$$

B. Extended wavepacket walker states and their optical implementation

As discussed above, attention must be paid to the beam radius of modes $|\mathbf{m}\rangle$. Indeed, once the lattice spacing Δk_\perp is fixed, w_0 must be selected so that the overlap between adjacent modes is negligible. In our set-up, $\Lambda = 5$ mm and our choice of setting the beam waist to $w_0 = 5$ mm leads to an overlap between adjacent modes of around 0.8%. In general, initial states other than localized ones can be prepared, such as for instance Gaussian wavepackets $|G\rangle = \mathcal{N} \sum_{\mathbf{m}} |\mathbf{m}\rangle e^{-(m_x^2 + m_y^2)/\sigma_G^2}$, where \mathcal{N} is a normalization factor and σ_G is the width of the overall Gaussian envelope (in dimensionless units). In Fig. S1, we plot a 1D cut of the corresponding beam-intensity wavevector profile versus k_x , at $k_y = 0$ (blue curve), showing several peaks modulated by a Gaussian envelope, each peak corresponding to a mode $|\mathbf{m}\rangle$ included in the wavepacket. The QW dynamics of such an input state is equivalent to that of a single Gaussian beam $|\Psi_g\rangle$, whose beam radius is $w_g = 2/(\sigma_G \Delta k_\perp)$. The preparation of such a state is much simpler, since it requires a modulation of the beam radius only, which is simply achieved with a confocal pair of lenses. In Fig. S1 we provide a comparison between the intensity distribution associated with $|G\rangle$ (blue curve) and $|\Psi_g\rangle$ (orange curve).

In our experiments, we are particularly interested at wavepackets $\mathcal{N} \sum_{\mathbf{m}} |\mathbf{m}\rangle e^{i\mathbf{q}_0 \cdot \mathbf{m}} e^{-(m_x^2 + m_y^2)/\sigma_G^2}$, that include the phase factor $e^{i\mathbf{q}_0 \cdot \mathbf{m}}$. Indeed, in quasi-momentum space these feature a Gaussian distribution with $\tilde{\sigma}_G = 2/\sigma_G$, peaked around a specific quasi-momentum \mathbf{q}_0 . Their expression reads

$$|\Psi_g(\mathbf{q}_0)\rangle = \mathcal{N}' \int_{\text{BZ}} \frac{d^2 \mathbf{q}}{4\pi^2} e^{-\frac{(\mathbf{q}-\mathbf{q}_0)^2}{\tilde{\sigma}_G^2}} |\mathbf{q}\rangle, \quad (S10)$$

where \mathcal{N}' is a normalization factor, and $\text{BZ} = [-\pi, \pi]^2$ is the Brillouin zone. We want these beams to be sharply peaked, that is $\tilde{\sigma}_G \ll 1$, so that they approximate as much as possible the individual state $|\mathbf{q}_0\rangle$. Being the simulated quasi-momentum encoded in the physical transverse position \mathbf{r}_\perp , these wavepackets are realized by standard Gaussian beams, whose central position is set to $\mathbf{r}_\perp = -\Lambda \mathbf{q}_0 / (2\pi)$, and which are characterized by a beam radius that is much smaller than the spatial period Λ .

In the focal plane of the lens, these beams display a continuous distribution, as shown for instance in Fig. 3b in the main manuscript. Being sharply peaked in the space of the walker quasi-momentum, we expect them to cover multiple lattice sites in the space of walker position. If one is interested in obtaining the associated walker probability distribution, our standard procedure described in Sec. S3 can be applied. However, in our experiments, we are interested in detecting the wavepacket center of mass, which can be determined by analyzing directly the overall intensity pattern recorded by the camera.

As shown in the main text, we use these beams to prepare photonic states:

$$|\Psi_g(\mathbf{q}_0, \pm)\rangle = |\Psi_g(\mathbf{q}_0)\rangle \otimes |\phi_\pm(\mathbf{q}_0)\rangle \quad (S11)$$

where the coin part corresponds to the eigenstates $|\phi_\pm(\mathbf{q}_0)\rangle$ of the effective Hamiltonian. These states are extremely useful to probe the QW dispersion and the associated topological features (see Figs. 3, 4 in the main manuscript).

2. DETAILS OF THE EXPERIMENTAL PLATFORM

A complete scheme of the set-up implementing our QW dynamics is reported in Fig. S2a. A laser beam is produced by a Helium:Neon source with wavelength $\lambda = 632.8$ nm, and propagates along the \hat{z} direction. We use a system of two lenses and a pinhole (L_1, Ph, L_2) to set the beam waist to $w_0 = (5.0 \pm 0.2)$ mm or to $w_0 = (0.62 \pm 0.02)$ mm, depending on our necessity to start the walk with either ‘‘localized states’’ or ‘‘extended wavepackets’’, respectively (see Sec. 1 for further details on the spatial features of the light beam). In the last stage of the preparation, a polarizer and two waveplates (P,H,Q) are used to prepare a given polarization.

The beam undergoes the proposed QW dynamics by passing through a sequence of wave-plates and g -plates. In panels b and c we display the combination of plates realizing the protocols U and U^{-1} , respectively. All operators are physically implemented by thin optical plates, which allows us to mount them in a very compact mechanical holder realized by a 3D printing technique. The distance between consecutive steps is currently $\simeq 2$ cm, yet it could be significantly reduced by optimizing the thickness of the glass and of the plastic mounts. Within each plate, the active layer containing liquid crystals (LCs) is $6 \mu\text{m}$ thick. The spatial period of g -plates pattern is $\Lambda = 5$ mm, yielding a transverse momentum displacement of $\Delta k_\perp = 2\pi/\Lambda = 1.26$ (mm) $^{-1}$, that provides the spacing between neighbouring sites in our squared lattice. In order to have each mode $|\mathbf{m}\rangle$ entirely localized on the associated site (m_x, m_y) , without ‘‘cross-talk’’, the single-mode beam radius w_0 must be properly selected. In Fourier space, where the lattice of walker positions is defined, these beams are characterized by a radius $w_k = \sqrt{2}/w_0$. If one chooses $w_0 \simeq \Lambda$, one gets that the ratio between the beam radius (in Fourier space) and the lattice spacing $w_k/\Delta k_\perp \simeq 1/\pi = 0.32$ is sufficiently small and the overlap between adjacent modes is negligible (see Fig. 1b in the main manuscript).

At the exit of the walk, two wave-plates and one polarizer (Q,H,P) are used to analyze individual polarization components. Finally a lens (L_3) focuses the field on a camera that records the distribution of light intensity, operating an all-optical Fourier transform. In the focal plane, light is spread over several spots, according to the walker distribution over the lattice. A single image contains the overall probability distribution, and the latter can be monitored in real time. Since the Rayleigh range of the input beam is much longer than the total distance of the walk

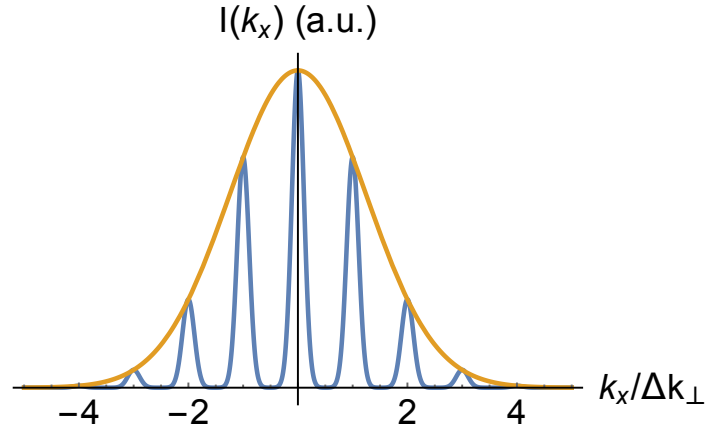


Fig. S1. Gaussian wavepackets. Comparison between the intensity distribution $I(k_x)$ (we set $k_y=0$) of the wavepacket states $|G\rangle$ (blue curve), with $\sigma_G = 2.5$, and of a single Gaussian mode $|\Psi_g\rangle$ (orange curve), whose beam radius in Fourier space is $\tilde{\sigma}_G = \sigma_G \Delta k_\perp$. In this plot, individual modes $|m\rangle$ contained in $|G\rangle$ are characterized by their actual beam radius $w_k = 0.23 \Delta k_\perp$.

(see Sec. 1), the latter takes place in the near field and the beam remains collimated.

3. EXTRACTION OF THE PROBABILITY DISTRIBUTIONS FROM THE INTENSITY PATTERNS

When injecting modes with beam radius $w_0 \simeq 5$ mm, at the end of the walk we record the light intensity in the focal plane of the camera, that is distributed over many spots corresponding to the walker lattice sites. The probability distribution of the associated quantum walk can be extracted by measuring the amount of light in each region. In principle, the lattice site positions on the camera could be determined by (i) individuating the axes origin $(0,0)$ (setting all g -plates at $\delta = 0$, so that a single spot appears on the camera), and (ii) determining the expected positions of the other sites in terms of the spacing Δk_\perp . However, imperfections of all plates can cause small deviations between actual spot positions and the expected ones. For instance, one contribution can be ascribed to undesired modulations in the g -plates patterns, that can be modelled by the local optic axis orientation $\alpha(x,y) = \alpha_0 + (\Delta k_\perp/2)x + \epsilon(x,y)$, where $\epsilon(x,y)$ is a small random error. Another source of errors can be a small tilt in the polarization gratings, so that the coordinate x in $\alpha(x)$ should be replaced by $x' = \cos(\theta)x + \sin(\theta)y$ (with θ small, and different for each grating).

To improve the calibration procedure, we follow therefore a different approach, which is illustrated in Fig. S3. Let us first consider the 1D set-up defined by the single step operator $U_x = T_x(\delta = \pi) \cdot H_{\text{wfp}}$, where H_{wfp} is a half-waveplate (that can be described by the operator σ_x). The particle dynamics, shown in Fig. S3a, is indeed very simple: at each step the positions of L/R polarized components are shifted respectively by ± 1 . If we start with a linearly polarized input beam, in the following steps we will see two spots (with opposite circular polarizations), which will be located, at the time t , at the effective positions $m_x = t$ and $m_x = -t$, respectively. In this way we reconstruct the coordinates of each site by performing Gaussian fits for the two spots. By repeating the same analysis with the protocol $U_y = T_y W$ we measure the y coordinate of each site. In the actual set-up, we can realize both protocols U_x and U_y by turning off ($\delta = 0$) plates T_x or T_y . After the site coordinates have been determined, we draw squared regions around each point (see Fig. S3b). Light detected within one of these regions is

automatically associated to the corresponding lattice sites. By integrating the light intensity measured within each square, and by dividing each of these values by their total sum, we obtain a properly normalized probability distribution for the walker position (see Fig. S3c).

4. OPERATORS IN QUASI-MOMENTUM SPACE AND DISPLACEMENT OF A WAVEPACKET IN THE PRESENCE OF A CONSTANT FORCE

We analyze the building blocks of the quantum walk in the reciprocal quasi-momentum space. For the W operator defined in Eq. 5 of the main text, the expression remains the same, as it does not depend on the position:

$$W = e^{i\frac{\pi}{4}\sigma_x} = \frac{1}{\sqrt{2}} \begin{pmatrix} 1 & i \\ i & 1 \end{pmatrix}, \quad (\text{S12})$$

where the basis of the polarization space has been chosen to be $\{|L\rangle, |R\rangle\}$.

The operator T_x can be obtained by the operator described in Eq. 2 in the main text. By inserting the explicit expression of the angle $\alpha(x) = x\pi/\Lambda + \alpha_0$, one obtains the expression of T_x in momentum space:

$$\begin{aligned} T_x(q_x) &= e^{i\frac{\delta}{2}(\cos(q_x)\sigma_x - \sin(q_x)\sigma_y)} = \\ &= \begin{pmatrix} \cos(\delta/2) & ie^{iq_x} \sin(\delta/2) \\ ie^{-iq_x} \sin(\delta/2) & \cos(\delta/2) \end{pmatrix}, \end{aligned} \quad (\text{S13})$$

and similarly for T_y :

$$\begin{aligned} T_y(q_y) &= e^{i\frac{\delta}{2}(\cos(q_y)\sigma_x - \sin(q_y)\sigma_y)} = \\ &= \begin{pmatrix} \cos(\delta/2) & ie^{iq_y} \sin(\delta/2) \\ ie^{-iq_y} \sin(\delta/2) & \cos(\delta/2) \end{pmatrix}, \end{aligned} \quad (\text{S14})$$

where we used the mapping $q_x = \frac{-2\pi x}{\Lambda}$, $q_y = \frac{-2\pi y}{\Lambda}$ and we set $\alpha_0 = 0$. This allows one to use the standard convention for the normalized plane waves:

$$\langle \mathbf{m} | \mathbf{q} \rangle = \frac{e^{i\mathbf{q} \cdot \mathbf{m}}}{2\pi}, \quad (\text{S15})$$

where \mathbf{q} is the quasi-momentum of the walker and \mathbf{m} is its position on the 2D lattice, according to the convention chosen in the paper.

As discussed in the main text, in quasi-momentum space the single step operator is

$$U(q_x, q_y, \delta) = T_y(q_y, \delta)T_x(q_x, \delta)W = \exp(-iH_{\text{eff}}(q_x, q_y, \delta)), \quad (\text{S16})$$

where $H_{\text{eff}}(\mathbf{q}) = \varepsilon(\mathbf{q})\mathbf{n}(\mathbf{q}) \cdot \sigma$ is the effective Hamiltonian, $\varepsilon(\mathbf{q})$ is the quasi-energy and $\mathbf{n}(\mathbf{q})$ is a unit vector representing the system eigenstates on the Bloch sphere. The quasi-energy $\varepsilon(\mathbf{q})$ is given by:

$$\cos \varepsilon = \frac{1}{\sqrt{2}} \left(A^2 - AB(\cos(q_x) + \cos(q_y)) - B^2 \cos(q_x - q_y) \right) \quad (\text{S17})$$

while the components of $\mathbf{n}(\mathbf{q})$ are

$$\begin{aligned} n_x &= \frac{-A^2 - AB(\cos(q_x) + \cos(q_y)) + B^2 \cos(q_x - q_y)}{\sqrt{2} \sin \varepsilon} \\ n_y &= \frac{-AB(\sin(q_x) + \sin(q_y)) + B^2 \sin(q_x - q_y)}{\sqrt{2} \sin \varepsilon} \\ n_z &= \frac{-AB(\sin(q_x) + \sin(q_y)) - B^2 \sin(q_x - q_y)}{\sqrt{2} \sin \varepsilon}. \end{aligned} \quad (\text{S18})$$

In these equations we defined the quantities $A = \cos(\delta/2)$ and $B = \sin(\delta/2)$. By looking at Eqs. S17-S18 it is clear that the effective Hamiltonian cannot be expressed as the sum of two terms acting along orthogonal directions, i.e., it is not separable.

The operator implementing the potential of the constant dimensionless force, $F_x \hat{m}_x$, can be regarded as a translation of the walker's quasi-momentum component q_x of a quantity F_x at each step. This operation is nondiagonal in momentum space, so the step operator in momentum space is described by $\langle \mathbf{q}' | \tilde{U}(t) | \mathbf{q} \rangle = \tilde{U}(\mathbf{q}', \mathbf{q}, t)$, where $\tilde{U}(\mathbf{q}', \mathbf{q}, t)$ is a 2×2 matrix operating in coin space only. In turn, the latter is given by $\tilde{U}(\mathbf{q}', \mathbf{q}, t) = \delta(q'_x - q_x + F_x t) \delta(q'_y - q_y) U(q_x + F_x t, q_y)$, where $\delta(\cdot)$ denotes a Dirac delta function and $U = e^{-iH_{\text{eff}}}$ is the step operator in coin space for a given quasi-momentum $\mathbf{q} = (q_x, q_y)$ for a vanishing force. We also have

$$U(q_x + F_x t, q_y) = T_y(q_y) e^{it \frac{F_x}{2} \sigma_z} T_x(q_x) e^{-it \frac{F_x}{2} \sigma_z} W. \quad (\text{S19})$$

The operator $e^{it \frac{F_x}{2} \sigma_z} T_x(\delta, \alpha_0) e^{-it \frac{F_x}{2} \sigma_z} = T_x(\delta, \alpha_0 - tF_x/2) = L(\delta, \pi x/\Lambda + \alpha_0 - tF_x/2)$ is obtained by shifting a g -plate by $\Delta x = tF_x \Lambda / (2\pi)$ along the x axis, which corresponds to the transformation $x \rightarrow x - \Delta x$. The same reference-system transformation realizes also the operation $q_x \rightarrow q_x + F_x t$ in quasi-momentum space.

In the adiabatic limit within the single band approximation, the semi-classical equations of motion of a wave-packet initially peaked around an energy eigenstate $e^{i\mathbf{q}_0 \cdot \mathbf{m}_0} |\phi_{\pm}(\mathbf{q}_0)\rangle$ read [1, 2]

$$\begin{aligned} \dot{m}_i &= \partial_{q_i} \varepsilon_{\pm}(\mathbf{q}) - \dot{q}_j \Omega_{ij}^{(\pm)}(\mathbf{q}), \\ \dot{q}_i &= F_i. \end{aligned} \quad (\text{S20})$$

Here $\{i, j\} \in \{x, y\}$, \pm denote the upper/lower band, $\varepsilon_{\pm}(\mathbf{q}) = \pm \varepsilon(\mathbf{q})$ is the quasi-energy dispersion and $\Omega_{ij}^{(\pm)}(\mathbf{q}) = -\Omega_{ji}^{(\pm)}(\mathbf{q})$ is the Berry curvature

$$\Omega_{xy}^{(\pm)}(\mathbf{q}) = i \left[\partial_{q_x} \langle \phi_{\pm}(\mathbf{q}) | \partial_{q_y} \phi_{\pm}(\mathbf{q}) \rangle - \partial_{q_y} \langle \phi_{\pm}(\mathbf{q}) | \partial_{q_x} \phi_{\pm}(\mathbf{q}) \rangle \right], \quad (\text{S21})$$

where the $|\phi_{\pm}\rangle$ are the eigenvectors of the Bloch effective Hamiltonian H_{eff}

$$H_{\text{eff}}(\mathbf{q}) |\phi_{\pm}(\mathbf{q})\rangle = \varepsilon_{\pm}(\mathbf{q}) |\phi_{\pm}(\mathbf{q})\rangle. \quad (\text{S22})$$

In our two-band system, the Berry curvature can also be written as [3]

$$\Omega_{xy}^{(\pm)}(\mathbf{q}) = \pm \frac{1}{2} \mathbf{n}(\mathbf{q}) \cdot \left[\frac{\partial \mathbf{n}}{\partial q_x} \times \frac{\partial \mathbf{n}}{\partial q_y} \right], \quad (\text{S23})$$

$\mathbf{n}(\mathbf{q})$ being the unitary vector giving the Floquet Hamiltonian $H_{\text{eff}}(\mathbf{q}) = \varepsilon(\mathbf{q})\mathbf{n}(\mathbf{q}) \cdot \sigma$. Therefore, for a force in the x -direction, the semi-classical equations of motion for a wavepacket center-of-mass read

$$\dot{m}_x^{(\pm)} = \partial_{q_x} \varepsilon_{\pm}(\mathbf{q}) \quad (\text{S24})$$

$$\dot{m}_y^{(\pm)} = \partial_{q_y} \varepsilon_{\pm}(\mathbf{q}) - F_x \Omega_{yx}^{(\pm)}(\mathbf{q}) = \partial_{q_y} \varepsilon_{\pm}(\mathbf{q}) + F_x \Omega_{xy}^{(\pm)}(\mathbf{q}). \quad (\text{S25})$$

We now sum the displacement of the wavepackets located on a grid $q_{x,y} = -\pi + 2\pi i/N$, where $i = 1 \dots N$. In the limit of $N \rightarrow \infty$, the mean displacement of the sum of the wavepackets corresponds to the average displacement of a filled band, i.e.,

$$\langle \Delta m_x(t) \rangle^{(\pm)} = 0 \quad (\text{S26})$$

$$\langle \Delta m_y(t) \rangle^{(\pm)} = \frac{F_x v^{(\pm)}}{2\pi} t, \quad (\text{S27})$$

where the Chern number of the \pm -th band is defined as:

$$v^{(\pm)} = \frac{1}{2\pi} \int_{\text{BZ}} d^2 \mathbf{q} \Omega_{xy}^{(\pm)}(\mathbf{q}), \quad (\text{S28})$$

One finds that the Chern number of the lower band for $\delta = \pi/2$ is $v^{(-)} = 1$, so that the displacement will be positive and proportional to time in the transverse direction for a positive force. By numerical tests, we have confirmed that a finite grid with 11×11 points in the BZ is sufficient in our system to obtain a good approximation of the continuous integral over the whole BZ.

As discussed in the main text, to provide a more accurate read-out of the Chern numbers of our QW, we also measured the displacements for the inverse protocol U^{-1} . This is obtained by properly tuning the plate retardations. Since $L(\delta_1)L(\delta_2) = L(\delta_1 + \delta_2)$ and $L(2\pi)$ is the identity operator (up to a global phase factor), the inverse operator is simply $L^{-1}(\delta) = L(2\pi - \delta)$. Recalling that $W = L(\pi/2, 0)$ [see Eq. 2 in the main text] and that $U = T_y(\delta)T_x(\delta)W$, it is straightforward to show that $U^{-1} = L(3/2\pi, 0)T_x(2\pi - \delta)T_y(2\pi - \delta)$.

5. TOPOLOGICAL CHARACTERIZATION

In static models, the bulk-edge correspondence guarantees that no edge modes may be present when all bands have trivial topological invariants. However, our QW protocol is described by an effective Floquet Hamiltonian. Depending on the values of δ , our effective Hamiltonian may or may not be deformed continuously into its static counterpart [4-6]. In particular, this can lead to regimes where the topological invariant of the static system, the Chern number, does not describe completely the

topology of the system and does not predict the presence of protected topological edge states.

In the present work, for example, we measured the anomalous displacement of the system for two values of the parameter δ , namely $\delta = \pi/2$ and $\delta = 7\pi/8$, associated respectively with Chern numbers $\nu^{(\mp)} = \pm 1$ and $\nu^{(\mp)} = 0$. As we will see in a few lines, the latter case displays protected edge modes, even though all its bands have trivial topological invariants.

The bulk-edge correspondence of such systems was studied in detail by Rudner *et al.* in Ref. [5]. In the specific case of our model, characterized by two bands which are symmetric around zero quasi-energy, edge states may appear independently within the gap centered at quasi-energy 0, or within the gap at quasi-energy $\pm\pi$. For definiteness, figure S4a shows the Chern number of the lowest band $\nu^{(-)}$, together with the topological invariants \mathcal{W}_0 and \mathcal{W}_π , which count, respectively, the number of pairs of edge modes in the 0-energy and π -energy gaps. Ref. [5] provides their analytical expression, which is rather involved, but nonetheless straightforward to compute.

To see the emergence of edge states, Figs. S4b,c,d show the spectrum of our model on a cylinder which is open (closed) along the direction x (y), for three values of the optical retardation $\delta = \pi/8, \pi/2$, and $7\pi/8$. In the vicinity of $\delta = 0$ both bands have trivial Chern numbers, and no edge states are visible (see Fig. S4b). As δ is increased further, a first gap closing happens at quasi-energy 0 when $\delta = \pi/4$. As the gap re-opens, a pair of protected edge modes appear around zero-energy, and the Chern numbers switch from 0 to ± 1 (see Fig. S4c). The next gap closing happens at quasi-energy $\pm\pi$ when $\delta = 3\pi/4$. Upon re-opening of this gap, another pair of protected edge modes appears inside it, and the Chern numbers switch back from ± 1 to 0 (see Fig. S4d).

The work by Rudner *et al.* [5] in particular showed that the Chern number is related to the number of 0 and π edge modes by $\nu^{(-)} = \mathcal{W}_0 - \mathcal{W}_\pi$. We computed numerically these invariants for our model, and we correspondently recovered the bulk-edge correspondence, as can be seen in Fig. S4a.

6. SUPPLEMENTARY DATA

In Figs. S5-S9, we show supplementary data supporting our results described in the main text.

7. POSSIBLE DEVIATIONS FROM THE IDEAL QW EVOLUTION

During propagation through the QW set-up, effects related to free space propagation of modes $|m\rangle$ can act as perturbations to the ideal QW dynamics. In this section we describe the main phenomena that can take place in our system, and investigate their effect with the help of a numerical analysis. For simplicity, we will refer to a 1D QW, where modes $|m\rangle$ are characterized by a single integer $m_x = m$.

There are essentially three “undesired” effects that may arise when considering the tilt in propagation direction *inside* the quantum walk:

1. At the end of the quantum walk, to each value of \mathbf{k}_\perp will correspond a superposition of waves that have followed different paths in the wavevector space, as illustrated in Fig. S10a. These trajectories are actually associated with different optical paths. Associated relative phases are absent in the ideal QW dynamics and can modify the interference of

the wavefunction components. To simulate this, the final amplitude of each mode $|m\rangle$ can be calculated as the sum of all components related to these optical paths, multiplied by their relative phase. When propagating between two consecutive timesteps, mode $|0\rangle$ and a different mode $|s\rangle$ accumulate a phase delay $\Delta\phi_1 \approx (\pi\lambda ds^2)/(\Lambda^2)$, where d is the distance between consecutive steps.

2. The two beams considered in Fig. S10a, that exit the walk in the same mode with $m = 0$, have an imperfect overlap that makes them partly distinguishable, since they are propagating along axes that are parallel but laterally displaced. These modes have a finite extension, and the absence of perfect spatial overlap results in a reduction of the interference visibility, similarly to a decoherence effect. Referring to the case presented above, between consecutive timesteps the two modes accumulate a lateral shift $|\Delta x| = d\lambda s/\Lambda$.
3. A tilted beam hits two consecutive g -plates at points that have a relative shift. Eq. 4 in the main text, describing the action of a g -plate, is derived by considering a Gaussian beam that hits the plate with its central position at $(x, y) = (0, 0)$. If the beam center is displaced by Δx , Eq. (4) in the main text remains valid after replacing α_0 with $\alpha'_0 = \alpha_0 + \Delta x \pi/\Lambda$, which represents the effective LC orientation at the beam central position. By looking at Eq. (4) in the main text, we can observe that this effect results in additional phases accumulated by modes $|m\rangle$ during propagation, which have to be added to the phases associated with the different path lengths (see the previous point 1).

All these effects are estimated to be negligible for our setup. To make a quantitative check, in Fig. S10b, we provide a comparison between an ideal QW evolution and the simulation of the real beam propagation through our set-up, by taking into account effects described in points (1-3) and using the real system parameters. After 10 steps of a 1D walk, we observe no significant deviations. This guarantees that also 5 steps of a 2D would not suffer any deviations. Indeed, such effects strongly depends on the typical order of the modes that are excited during the walk, which is of course limited by the highest possible order. In the first case, when starting from a localized input, the highest-order mode that can be excited has $|m| = \pm 10$. In the 2D case, highest-order excited modes have $|m| = \sqrt{m_x^2 + m_y^2} = 5\sqrt{2} \approx 7$.

In prospect, when increasing the number of steps, we expect these systematic deviations from ideality to become progressively more relevant. On the other hand, if needed, these issues could be tackled by (i) changing the system parameters, in particular increasing Λ and reducing the step distance d , or (ii) by adopting a loop architecture combined with an imaging system. Indeed, by imaging the output of each step to the input of the following one, all the effects discussed above can be eliminated.

REFERENCES

1. H. M. Price, O. Zeitler, T. Ozawa, I. Carusotto, and N. Goldman, “Measurement of chern numbers through center-of-mass responses,” *Phys. Rev. B* **93**, 245113 (2016).
2. A. Dauphin and N. Goldman, “Extracting the chern number from the dynamics of a fermi gas: Implementing a quantum hall bar for cold atoms,” *Phys. Rev. Lett.* **111**, 135302 (2013).

3. X.-L. Qi, T. L. Hughes, and S.-C. Zhang, "Topological field theory of time-reversal invariant insulators," *Phys. Rev. B* **78**, 195424 (2008).
4. F. Cardano, A. D'Errico, A. Dauphin, M. Maffei, B. Piccirillo, C. de Lisio, G. De Filippis, V. Cataudella, E. Santamato, L. Marrucci, M. Lewenstein, and P. Massignan, "Detection of Zak phases and topological invariants in a chiral quantum walk of twisted photons," *Nat. Commun.* **8**, 15516 (2017).
5. M. S. Rudner, N. H. Lindner, E. Berg, and M. Levin, "Anomalous edge states and the bulk-edge correspondence for periodically driven two-dimensional systems," *Phys. Rev. X* **3**, 031005 (2013).
6. F. Nathan and M. S. Rudner, "Topological singularities and the general classification of floquet-bloch systems," *New J. Phys.* **17**, 125014 (2015).

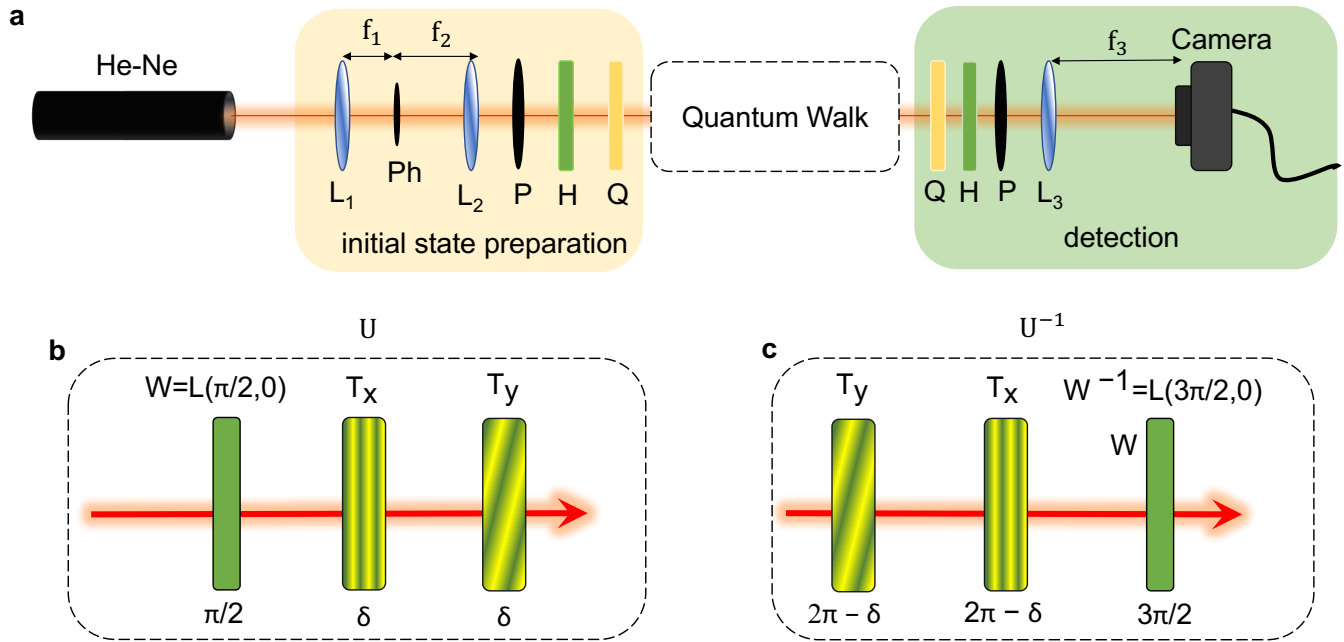


Fig. S2. Details of the experimental set-up and protocols. **a.** Sketch of the experimental set-up. The waist of a laser beam emitted from a He-Ne laser is modified with a pair of convex lenses L_1 and L_2 , with focal lengths f_1 and f_2 . A pinhole (Ph), placed in the common focus of the two lenses, is used as spatial filter to erase higher-order spatial frequencies. The polarization of the input state is selected by means of a polarizer (P), a half-wave plate (H) and a quarter-wave plate (Q). These wave plates are mounted on motorized rotation stages allowing for automatic selection of the coin states. After the QW an additional set of waveplates can be used to analyze the probability distributions of specific polarization components. The probability distribution is visualized by focusing the laser beam on a camera with a lens L_3 of focal length $f_3 = 50$ cm. **b.** A single step of our QW with protocol U is obtained by cascading three optical plates: a spin rotation W , followed by a coin-conditioned translation along x and another along y , with optical retardations δ as indicated below every device. **c.** Set-up yielding a single step of the inverse protocol U^{-1} .

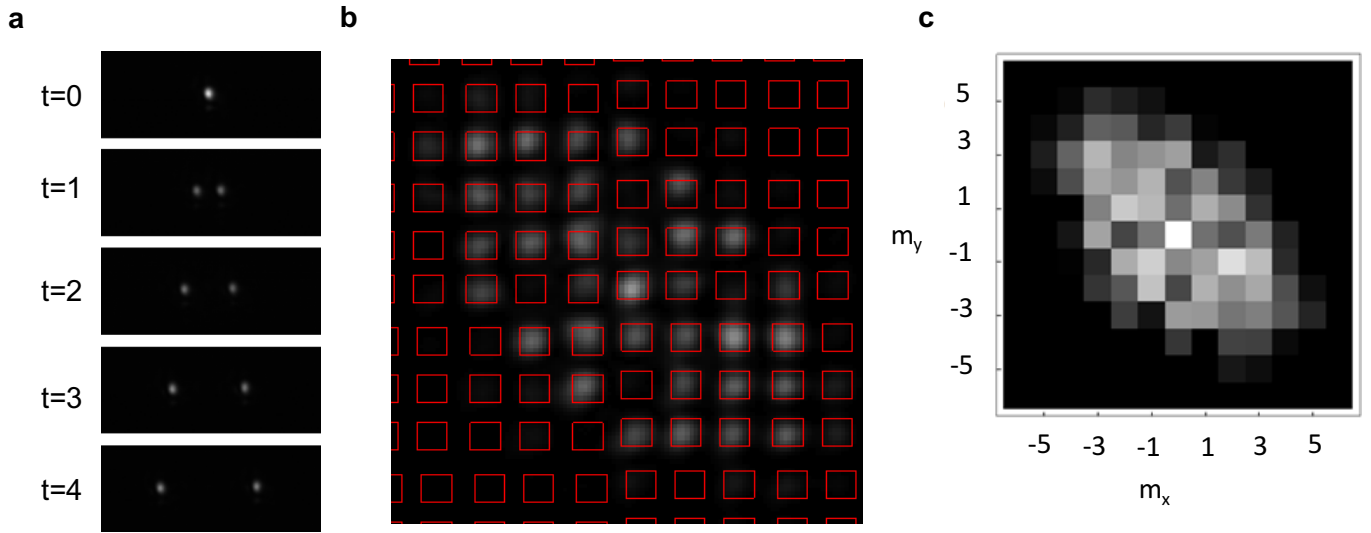


Fig. S3. Extracting probability distributions from the recorded intensity patterns. **a**, Sample intensity patterns obtained with the simple protocol $U = S_x(\pi) \cdot H_{wp}$. An input linearly polarized state is split into two spots with opposite circular polarizations. At each step these spots are shifted by a quantity corresponding to the equivalent of a lattice spacing. This process can be used to identify the coordinates of the lattice sites on the camera, getting rid of some of the experimental imperfections explained in the text. Panels **b** and **c** show the procedure used to extract the probability distributions from the intensity patterns. The red squares in **b** represent the regions over which we obtain the total intensities (= powers) associated to specific lattice sites (since the single spots occupy a small number of pixels there is no substantial difference in using square or circular integration regions). Normalizing to 1 the sum of all these intensities we obtain the probability distribution shown in panel **c**.

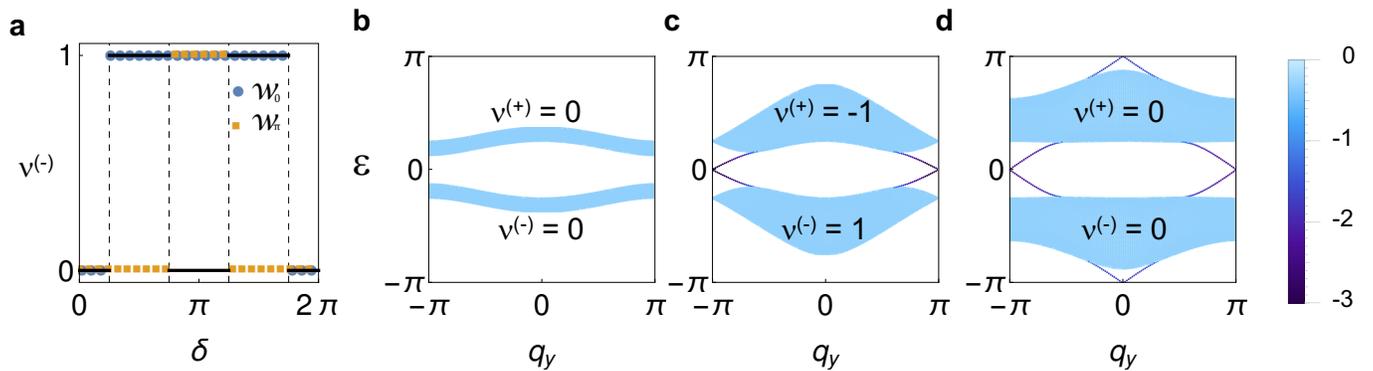


Fig. S4. Complete topological characterization of the QW protocol and bulk-edge correspondence. **a**, Phase diagram of our QW protocol showing the Chern number ν and the topological invariants $\mathcal{W}_0, \mathcal{W}_\pi$ defined in Ref. [5]. **b-c-d**, Quasi-energy spectra computed on a cylinder open along x for $\delta = \pi/8$ (**b**), $\delta = \pi/2$ (**c**) and $\delta = 7\pi/8$ (**d**). The color scale depicts the function $\lambda = \log_{10}(1 - \langle |\hat{x}| \rangle_\psi / N)$, which indicates the degree of localization of each state ψ . The two edges of the cylinder are located at $m_x = -N$ and $m_x = N$, so that lighter points denote bulk states, while darker points denote states that are closer to the edges.

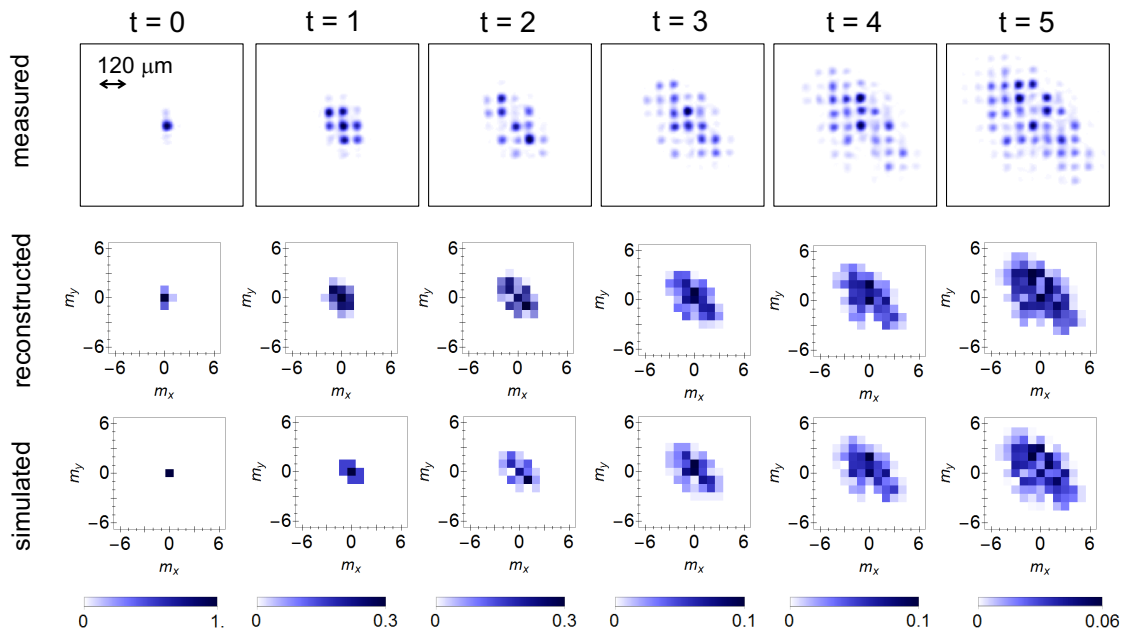


Fig. S5. 2D QW for input polarization $|A\rangle = (|L\rangle - i|R\rangle)/\sqrt{2}$. Spatial probability distributions for a quantum walk with initial condition $|0, 0, A\rangle$ and optical retardation $\delta = \pi/2$. From left to right, we display results after 0 to 5 evolution steps. Datapoints are averages of four independent measures.

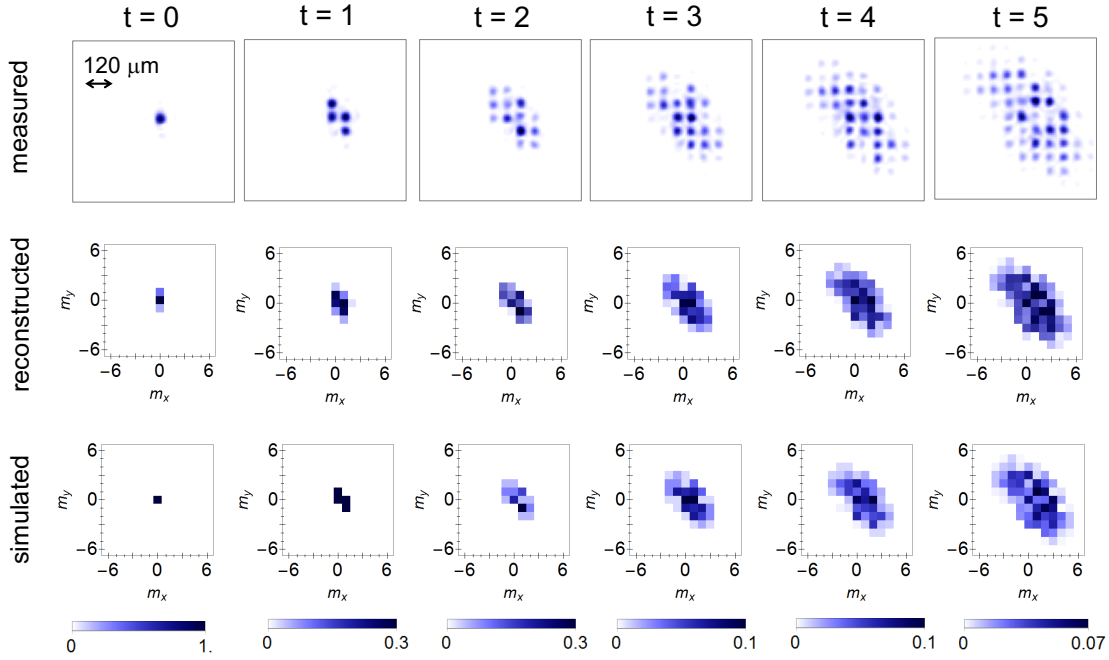


Fig. S6. 2D QW for input polarization $|L\rangle$. Spatial probability distributions for a quantum walk with initial condition $|0, 0, L\rangle$ and optical retardation $\delta = \pi/2$. From left to right, we display results after 0 to 5 evolution steps. Datapoints are averages of four independent measures.

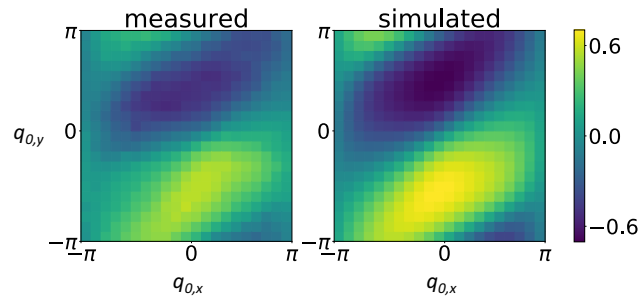


Fig. S7. Group velocity detection. Measurement of the y component of the group velocity $\mathbf{v}^{(+)}$, for the upper band of a QW with $\delta = \pi/2$. Each datapoint is obtained from a linear fit of the center of mass displacement of a Gaussian wavepacket.

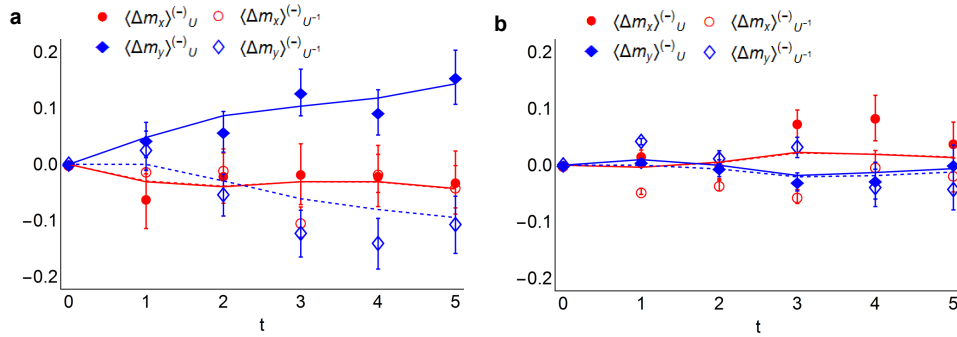


Fig. S8. Anomalous and individual displacements for protocols U and U^{-1} We report experimental data compared with theoretical simulations of the wavepacket evolution of the anomalous $\langle \Delta m_y \rangle^{(-)}$ and longitudinal $\langle \Delta m_x \rangle^{(-)}$ displacements, obtained for the protocols U and its inverse U^{-1} . **a** Results for $\delta = \pi$. **b** Results for $\delta = 7\pi/8$. In both panels the blue lines correspond to simulations for displacements along y (continuous line for U and dashed for U^{-1}) while the red lines are simulations for displacement along x (continuous line for U and dashed for U^{-1}). Subtraction of these data allows to retrieve the results in Fig. 4 of the main text.

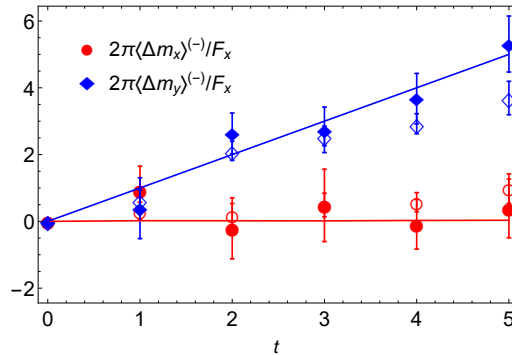


Fig. S9. Wavepacket displacements for larger values of the force. Band-averaged wavepacket displacements in the x and y directions, for $F = \pi/10$ (filled markers) and $F = \pi/5$ (empty markers), obtained combining measurements from the direct and inverse protocols, with $\delta = \pi/2$, for the lower band. Datapoints are experimental data, the continuous lines represent semi-classical predictions.

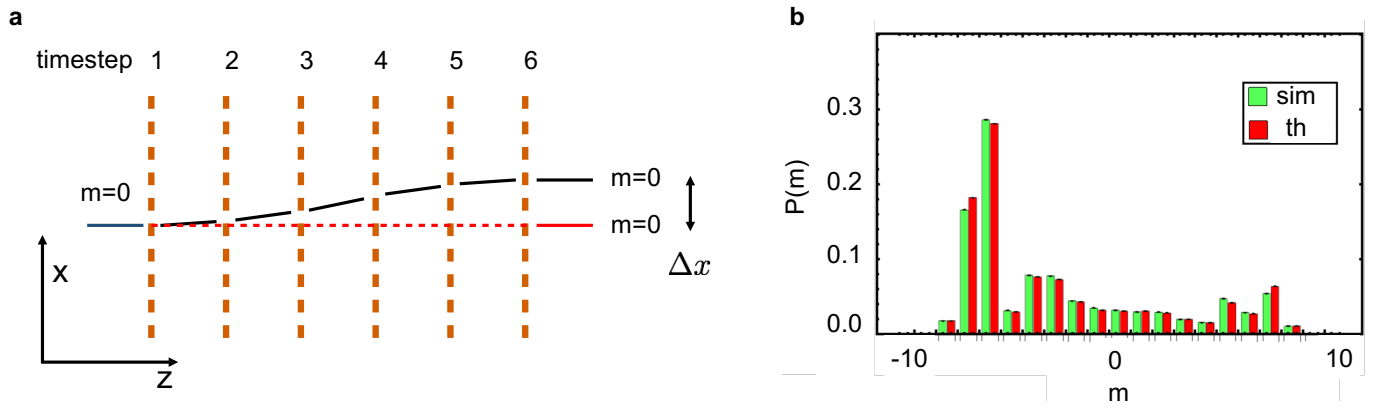


Fig. S10. Deviations from the perfect simulation of a QW process. **a**, At the input of the 1D QW we have a single beam with $\mathbf{k}_\perp = 0$, localized at the lattice site $m = 0$. At the exit of a 6-steps QW, we consider two contributions to the final wavefunction at site $m = 0$. One is resulting from the part of the input state that has been left unchanged (red). The second has gained Δk transverse momentum at the first three steps, and then has acquired opposite momentum at steps 4 to 6 (black). At the exit of the walk, also this component corresponds to the lattice site $m = 0$. However, the associated beams have some differences, which represent deviations from the ideal QW; being related to the same lattice site, they should be identical. First, they exit the walk laterally displaced by Δx , and the lack of overlap may reduce the interference, similarly to a decoherence effect. Second, the upper beam suffered a longer optical path, hence it accumulated a relative phase with respect to the central one. Finally, at each g -plate, the effective value of α_0 changes at each step for the deflected beam. **b**, Numerical simulation of a 1D walk with protocol $U = T_x W$, for $\delta = \pi/2$ and for an input state $|0, R\rangle$ (green columns), compared to a theoretical predictions of the ideal QW dynamics (red columns). After 10 steps differences are minimal.